The impact of system matrix dimension on small FOV SPECT reconstruction with truncated projections

Chung Chan[a)]
Department of Diagnostic Radiology, Yale University, New Haven, Connecticut 06520

Joyoni Dey
Department of Physics and Astronomy, Medical Physics Program, Louisiana State University, Baton Rouge, Louisiana 70803

Yariv Grobshtein
GE Healthcare, Haifa 30200, Israel

Jing Wu
Department of Diagnostic Radiology, Yale University, New Haven, Connecticut 06520

Yi-Hwa Liu and Rachel Lampert
Department of Internal Medicine, Yale University, New Haven, Connecticut 06520

Albert J. Sinusas
Department of Diagnostic Radiology, Yale University, New Haven, Connecticut 06520 and Department of Internal Medicine, Yale University, New Haven, Connecticut 06520

Chi Liu[a)]
Department of Diagnostic Radiology, Yale University, New Haven, Connecticut 06520

(Received 15 May 2015; revised 2 October 2015; accepted for publication 25 November 2015; published 23 December 2015)

Purpose: A dedicated cardiac hybrid single photon emission computed tomography (SPECT)/CT scanner that uses cadmium zinc telluride detectors and multiple pinhole collimators for stationary acquisition offers many advantages. However, the impact of the reconstruction system matrix (SM) dimension on the reconstructed image quality from truncated projections and 19 angular samples acquired on this scanner has not been extensively investigated. In this study, the authors aimed to investigate the impact of the dimensions of SM and the use of body contour derived from adjunctive CT imaging as an object support in reconstruction on this scanner, in relation to background extracardiac activity.

Methods: The authors first simulated a generic SPECT/CT system to image four NCAT phantoms with various levels of extracardiac activity and compared the reconstructions using SM in different dimensions and with/without body contour as a support for quantitative evaluations. The authors then compared the reconstructions of 18 patient studies, which were acquired on a GE Discovery NM570c scanner following injection of different radiotracers, including ^{99m}Tc-Tetrofosmin and ^{123}I-mIBG, comparing the scanner's default SM that incompletely covers the body with a large SM that incorporates a patient specific full body contour.

Results: The simulation studies showed that the reconstructions using a SM that only partially covers the body yielded artifacts on the edge of the field of view (FOV), overestimation of activity and increased nonuniformity in the blood pool for the phantoms with higher relative levels of extracardiac activity. However, the impact on the quantitative accuracy in the high activity region, such as the myocardium, was subtle. On the other hand, an excessively large SM that enclosed the entire body alleviated the artifacts and reduced overestimation in the blood pool, but yielded slight underestimation in myocardium and defect regions. The reconstruction using the larger SM with body contour yielded the most quantitatively accurate results in all the regions of interest for a range of uptake levels in the extracardiac regions. In patient studies, the SM incorporating patient specific body contour minimized extracardiac artifacts, yielded similar myocardial activity, lower blood pool activity, and subsequently improved myocardium-to-blood pool contrast ($p < 0.0001$) by an average of 7% (range 0%–18%) across all the patients, compared to the reconstructions using the scanner's default SM.

Conclusions: Their results demonstrate that using a large SM that incorporates a CT derived body contour in the reconstruction could improve quantitative accuracy within the FOV for clinical studies with high extracardiac activity. [http://dx.doi.org/10.1118/1.4938098]

Key words: SPECT/CT, projection truncation, small field-of-view, dedicated cardiac SPECT, SPECT reconstruction

1. INTRODUCTION

Dedicated cardiac single photon emission computed tomography (SPECT) systems have recently emerged for clinical imaging.[1,2] These systems commonly use small detectors and constrain the focus of the detector area primarily to the heart. A particular interesting SPECT detector configuration was developed that uses 19 cadmium zinc telluride (CZT) detectors with pinhole collimators (Discovery NM530/570c, GE Healthcare) to acquire all image projections simultaneously without moving or rotating the camera during acquisition. This novel SPECT system configuration provides a fully stationary geometry for acquiring 3D images.[3] A 64-slice CT scanner has also been incorporated to the SPECT system to form a hybrid SPECT/CT system (Discovery NM570c, GE Healthcare) that facilitates both attenuation correction and anatomical localization. This system has been reported to improve sensitivity by 3–4-fold, spatial resolution by 1.7–2.5-fold, and energy resolution by 2-fold compared to conventional dual head NaI SPECT systems.[1,3] The stationary acquisition also provides consistent angular data that allow dynamic imaging,[4] respiratory gating, and dual respiratory/cardiac gating to reduce motion blurring during cardiac SPECT imaging.[5]

However, the dedicated cardiac CZT SPECT systems have a smaller focused field of view (FOV) [~19 cm diameter on the GE Discovery NM 530c/570c (Ref. 3)] that covers primarily the heart, potentially causing projection truncation, particularly for patients with larger body size. This effect is caused by the fact that activities outside the FOV, such as background activity from other adjacent organs, are imaged by some but not all detectors.[6–9] Reconstructions of data with projection truncation could yield artifacts such as high intensity value on the edge of the FOV, and bias within the FOV in the reconstructed images.[7,10,11] However, the reported impact of projection truncation on SPECT image quality has varied in the literature. Using simulation studies and a fan beam cardiac SPECT system, Gregoriou *et al.* demonstrated that the impact of truncation on defect detection only became noticeable when the lateral dimension of the detector was smaller than 60% of the lateral width of the patient thorax.[12] Zeniya *et al.* using a synthetic cylindrical phantom and simulations of data acquisition from a single pinhole collimator that rotated 360°, demonstrated that projection truncation produced up to 23% overestimation in the image, depending on the level of background activity.[13,14] Sabodjian *et al.* simulated a small FOV system (16×16 cm) by artificially truncating the data from patient studies acquired on a two-head GE Infinia-Hawkeye system, and showed that the reconstructions of the truncated projections yielded over 100% overestimation in the myocardium, and on average a 17% reduction in defect size.[15] Xiao *et al.*, on the other hand, investigated the impact of truncations that occurred only in the axial direction. Their results suggested that the impact of truncations on single isotope SPECT was insignificant and should not affect clinical diagnosis.[16]

To achieve exact and stable region-of-interest (ROI) reconstruction from truncated projections, Defrise *et al.*[17] defined generalized sufficient conditions for tomographic systems. First, the FOV must contain the edge of the support of the object, such that the background count is null or a known value. Second, the target ROI must lie within the FOV of the detector at every position along a 180° trajectory. For pinhole collimation, only the portion of the FOV that overlaps with the convex hull determined by the pinhole geometry satisfies this condition.[18] Third, for iterative methods, the system matrix (SM) must be large enough to contain the entire object even if only a ROI is to be reconstructed. In addition, with the fulfillment of these conditions, studies also demonstrated that the use of body contour as a support in reconstruction could effectively reduce bias and artifacts caused by projection truncation in both transmission[9,19] and emission[12,15,20] applications. A more recent study suggested that when projections are truncated, sufficient angular sampling (e.g., >60 views over 180° rotation) is required to have a quantitative and artifact free reconstruction, otherwise the solution is not unique even when a subregion value is known as *a priori* knowledge.[21] Later work from the same group proposed a tailored maximum likelihood expectation maximization (MLEM) reconstruction algorithm that reduced artifacts in the reconstructed images from truncated projections and sparse angular sampling for a parallel-hole SPECT scanner.[22]

The previously established sufficient conditions might not have the same effects on stationary dedicated cardiac SPECT systems with 19 pinhole collimators as used in one of the clinical cardiac CZT SPECT systems. In addition, the critical effect of the dimensions of the SM on quantitative reconstruction has not been thoroughly studied in the literature. Although it has been suggested that the SM should be large enough to enclose the whole support of the object, if an excessive large SM is used to fit all types of patients, it may also cause bias in the reconstruction as the radioactivity can be artificially back-projected beyond the body in the reconstruction. Furthermore, the use of body contour as a support in the reconstruction has been demonstrated to alleviate most of the artifacts in simulation studies previously. Whether this technique can yield quantitative results for different tracers and levels of extracardiac activity on this SPECT geometry has not been investigated previously.

In this study, with the emphasize on quantification tasks, we aim to investigate the impact of the dimension of SM and the use of body contour as a support in image reconstruction for a dedicated cardiac hybrid SPECT/CT. We first simulated a generic SPECT/CT system to image four NCAT phantoms with various levels of extracardiac activity for quantitative evaluation of cardiac activity. We then investigated the reconstructions incorporating patient specific body contour

in comparison with the system default SM that covers the majority of the body in 18 patient studies acquired on a GE Discovery NM570c scanner.

2. MATERIALS AND METHODS

2.A. Multiple pinholes SPECT systems in simulation studies

The dedicated cardiac SPECT system was simulated with multiple pinholes collimators and pixelated detector modules. The geometry of the collimator setting was similar to the system proposed by Dey.[23] The system was fully stationary with 27 pinholes arranged on a cylindrical surface in 3 columns. Each column had nine pinholes evenly distributed across 180°, and all the pinholes focused on the heart, as illustrated in Figs. 1(a) and 1(b). The quality FOV of the system was 21 cm in diameter and represents the volume that can be seen by all the detectors. This FOV is illustrated by the green sphere in Fig. 1. The distance from pinhole aperture to the detector was fixed at 6 cm, and the distance between the pinhole aperture and the center of the FOV was 16 cm. The pinhole radius and acceptance angle was set to 0.2 cm and 67°, respectively. The radius of the CZT detector base was set to 8 cm, which is composed of 32 × 32 pixelated detectors with 0.25 cm dimensions, similar to the GE Discovery NM 530/570 systems.[3] A nontruncated CT module was assumed to provide coregistered CT images as *a priori* knowledge of the object support for reconstruction. This concept will be expanded on in Sec. 2.E. The detailed implementation of this generic scanner can be found in the work of Dey.[24] Depth dependent attenuation factors and pinhole sensitivity were modelled in the simulation. For each emitted projection ray, a Siddon-ray-tracing method was used to obtain the path lengths l_i through all the voxels intersected by the projection ray in the path from the originating voxel to the pinhole. The projection is then multiplied by the net attenuation factor $\exp(-\sum_j \mu_j l_j)$, where μ_j is the linear attenuation coefficients for the jth voxel, for the gamma-ray energy considered. The pinhole sensitivity is also accounted for in the projector as previously described.[24,25] To isolate the quantification bias caused by projection truncation, scatter and collimator detector response were not simulated.

2.B. Human imaging studies with GE Discovery NM530/570c system

All the patient studies were acquired on a GE Discovery NM 570c SPECT scanner installed at Yale New Haven Hospital. This system employs 19 detector modules, each of them consists of 4 pixelated solid-state CZT detectors, placed behind a single aperture (5 mm) pinhole collimator. The detector modules are arranged in three columns, where the central column consists of nine detector modules, and the other outer two columns located on each side consist of five detector modules.[26] The detector modules are arranged on an L shaped arc that covers nearly 180° around the patient. Each of these modules yields a projection in a 32 × 32 matrix with 2.46 × 2.46 mm pixels. All the 19 pinhole collimators are focused on a spherical FOV with 19 cm in diameter to perform stationary SPECT imaging.[3]

2.C. Simulations

To investigate the impact of projection truncation in relation to the extra FOV activity, and to assess the robustness of using body contour in reconstruction, we generated 4 NCAT phantoms with the same body size but different levels of background activity as shown in Fig. 2. The lateral thorax width of the phantom is 34 cm and the heart is positioned at the center of FOV and is covered by all the projections as illustrated in Fig. 1(a). However, a significant portion of the NCAT phantom including the right lung and the liver are outside the quality FOV (the green sphere) on the simulated system. The uptake ratios between the myocardium and the rest of the organs were varied to simulate realistic ^{99m}Tc-Tetrofosmin myocardial perfusion scans (phantoms 1 and 2)[27] and ^{123}I-metaiodobenzylguanidine (^{123}I-mIBG) cardiac studies (phantoms 3 and 4).[28] A summary of the distributions

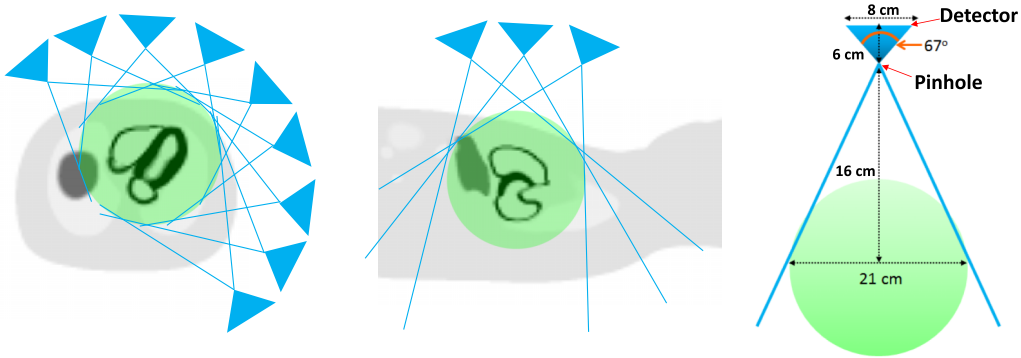

FIG. 1. Design of the dedicated cardiac multiple pinhole SPECT scanner. (a) This diagram illustrates how nine pinholes surrounding a NCAT phantom are all simultaneously imaging the heart in transaxial view. The green sphere presents the FOV of the scanner. The pinhole apertures are distributed on a cylindrical surface with a radius of 16 cm. (b) The pinhole collimators shown in longitudinal axis. (c) Profile of a single detector on a pinhole.

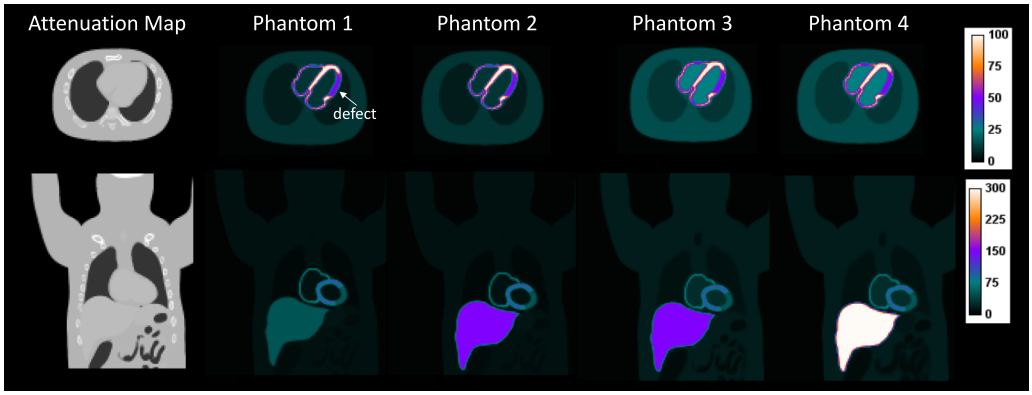

FIG. 2. Simulated NCAT phantoms shown in transaxial (top) and coronal (bottom) views. Note that different color scale is used to display the coronal images to illustrate the different distributions of extracardiac activity.

of radioactivity in each organ is shown in Table I. A transmural defect with a 50% reduction of the myocardial radioactivity was also inserted in all the phantoms. The defect extended over 120° of the total width in the circumferential dimension and from the apex to the base in the long-axis dimension in the lateral wall. The uptake in all organs was assumed to be uniformly distributed. The attenuation map shown in Fig. 2 was used in all the simulations and reconstructions. Noiseless projections were acquired to isolate the bias and nonuniformity caused solely by the geometric factors from statistical noise.

2.D. Patient studies

Fourteen patients (11 male and 3 female) who were referred for clinical ^{99m}Tc-Tetrofosmin myocardial perfusion SPECT imaging or research ^{123}I-mIBG cardiac sympathetic imaging were retrospectively reprocessed. Four patients underwent both stress and rest myocardial perfusion scans, and ten patients had only a single stress or rest scan, thus providing a total of 18 patient studies in total for analysis. Among all the studies, 15 were acquired after injection of ^{99m}Tc-Tetrofosmin and three following injection of ^{123}I-mIBG. The reprocessing of anonymized clinical studies was approved by our institutional review board (IRB).

2.E. Reconstructions

In this study, four SMs with different sizes were investigated with the simulated phantoms as illustrated in Fig. 3. The center of the SM is located at the center of the rectangular box in Fig. 3. The first SM reconstructed the image into a 60 × 60 × 128 grid, which covers just the FOV and is referred as SM60 in the following context. In the second configuration, we extended the SM to yield a reconstruction volume of 70 × 70 × 128 (SM70), which covers the majority of the body. The size of the SM70 is close to the default SM in the commercial software on the GE Discovery 530c/570c workstation. Note for these two sizes of SM, the truncation was mainly in the transaxial plane, but not in the axial direction. The attenuation map is also truncated the same way to match the dimension of SM60 and SM70 as illustrated in Figs. 3(a) and 3(b). In the third configuration, we generated an excessively large SM that reconstructed images into a volume of 128 × 128 × 128 (SM128). This system matrix is large enough to ensure that the entire object is fully contained. In the last setting, SM128 was used along with a body contour obtained from CT attenuation map as the support in the reconstruction. This was achieved by setting the voxels inside the body contour to one, and otherwise to zero in the initial image. This reconstruction scheme is named SM128-BC. For SM128 and SM128-BC, the complete attenuation map was used in the reconstructions. All the data were reconstructed using 3D MLEM reconstruction algorithm[29] into a 4 mm voxel grid with 150 iterations. The images derived from every 10th iteration were used in the quantitative evaluations, as will be discussed in Sec. 2.F. All the images displayed in the figures were from the 100th iteration.

For the patient studies, two reconstruction schemes were investigated including the default SM that reconstructs images into a dimension of 70 × 70 × 50 (SM70), and a customized SM that produces images of 150 × 150 × 150 incorporating a patient specific body contour as the support in reconstruction (SM150-BC). These system matrices and associated collimator detector responses were both generated by the manufacturer (GE Healthcare, Haifa, Israel) and incorporated into an ordinary MLEM (Ref. 29) reconstruction program developed at Yale. The raw data were first rebinned into projections on the GE Xeleris™ workstation using the listmode processing software (Lister™, GE Healthcare). A 10% symmetrical energy window centered at the peak energy spectrum of each radiotracer was applied during the rebinning process. The rebinned projections were then exported for offline reconstruction. Attenuation correction

TABLE I. The summary of the relative radioactivity concentration in each organ.

	Myo	Defect	Blood pool	Liver	Gall bladder	Lung	Body
Phantom 1	100	50	10	50	50	5	10
Phantom 2	100	50	10	150	150	5	10
Phantom 3	100	50	25	150	150	10	15
Phantom 4	100	50	25	300	300	10	15

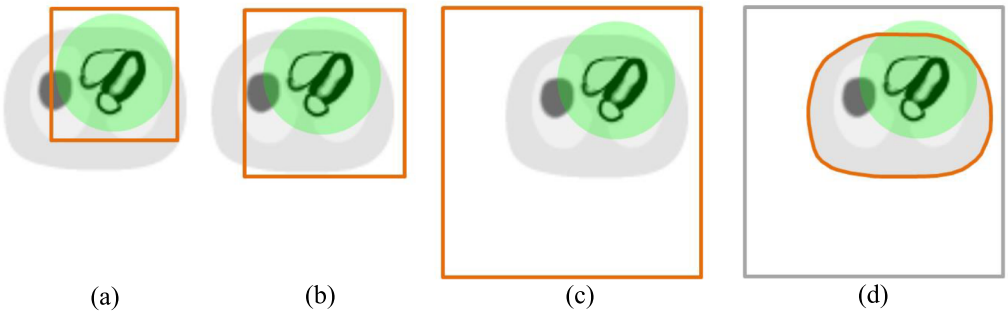

FIG. 3. Illustration of the reconstruction schemes using different SMs. The semitransparent sphere (green) overlayed on the NCAT phantom illustrates the FOV of the simulated system. The solid bold boundary illustrates the effective reconstruction region in the transaxial view. (a) SM60 represents reconstruction of images into $60 \times 60 \times 128$ matrix, which covers just the FOV. (b) SM70 represents reconstruction of images into $70 \times 70 \times 128$ matrix, which covers the majority of the body. (c) SM128 represents an excessively large reconstruction matrix ($128 \times 128 \times 128$) that covers the entire object. (d) SM128-BC represents the use of the same image matrix as (c) but constrains the reconstruction within the body contour obtained from a CT attenuation map.

was incorporated in the reconstruction. All the images were reconstructed on a 4 mm voxel grid with 100 iterations. The body contour of each patient was obtained by applying an adaptive thresholding after cropping out the beds from the attenuation map manually. Note unlike the simulation studies, the patient studies were truncated in both the transaxial and axial directions. We did not reconstruct images using the large SM ($150 \times 150 \times 150$) without BC as there would be missing attenuation on both sides in the axial direction (the FOV of the attenuation CT matches with the SPECT FOV in the axial direction). A postreconstruction Butterworth filter was applied to the patient images using a cutoff frequency of 0.37 cycles/cm and order of 7. Note that the one-step-late MAP algorithm using SM70 is the clinical default reconstruction on the vendor's workstation,[3] which is different from MLEM used in our offline reconstruction in this study.

2.F. Data analysis

For the simulated phantoms, we calculated the regional Bias and coefficient of variation (CoV) in normal myocardium, defect, and blood pool. These ROIs were defined as the entire structure on the phantom. The Bias-CoV comparison curves were generated across 150 iterations, and each data point represents an increment of 10 iterations. This figure-of-merit computed from noiseless images can give us insights into bias and variation introduced by the combination of projection truncations and the use of suboptimal reconstruction matrices. The bias and COV are defined as below

$$\mu_{\mathrm{ROI}} = \frac{1}{R} \sum_{r \in \mathrm{ROI}} f_r, \tag{1}$$

$$\mathrm{Bias} = \frac{\mu_{\mathrm{ROI}} - \mu^T_{\mathrm{ROI}}}{\mu^T_{\mathrm{ROI}}} \times 100\%, \tag{2}$$

$$\mathrm{CoV} = \frac{\sqrt{\frac{1}{R-1} \sum_{r=1}^{R} (f_r - \mu_{\mathrm{ROI}})^2}}{\mu_{\mathrm{ROI}}} \times 100\%, \tag{3}$$

where μ_{ROI} is the mean activity inside a ROI, f_r is voxel r within the ROI, R is the total number of voxels within the ROI, and μ^T_{ROI} is the mean intensity within the ROI of the true image.

To quantitatively assess the reconstructions of the patient studies, we computed the mean activities in the myocardium and blood pool and the contrast between myocardium and blood pool for 18 studies. The ROIs were drawn manually on the myocardium and blood pool on the SA view, and the mean activity was averaged across three central slices.

3. RESULTS

3.A. Simulations

Figure 4 presents the central transaxial slices of the noiseless NCAT phantoms reconstructed with different reconstruction schemes (columns). Each row reflects the impact of SM on the reconstructions from the same projections. Each column reflects the impact of projection truncation from different intensities of extracardiac activity relative to the heart on the same SM. For phantoms 1 and 2, it can be observed that all system matrices yielded similar image quality within the FOV. However, SM60 yielded bright spots on the edge of the reconstruction FOV, as denoted by the dashed arrow. The larger system matrices (from left to right, SM70, SM128, and SM128-BC) eliminated the artifacts. For phantoms 3 and 4 that had higher background activity (blood pool, lung, and body), the artifacts in the image reconstructed with SM60 are more severe and demonstrated increased nonuniformity in the left ventricle and high intensity structures in the left ventricular blood pool. SM70 alleviated the artifactual elevated uptake in the left blood pool. SM128 and SM128-BC yielded image quality close to the ground truth. These results demonstrate that the reconstruction using large SMs is more robust to different levels of background activities, even with projection truncations and discrete pinhole angular sampling present in the small FOV cardiac CZT imaging system.

Figure 5 shows the percentage bias vs percentage CoV plots of the simulations. The CoV calculated from noiseless data is used to assess the nonuniformity introduced by using a suboptimal SM in the reconstruction. It can be seen that in

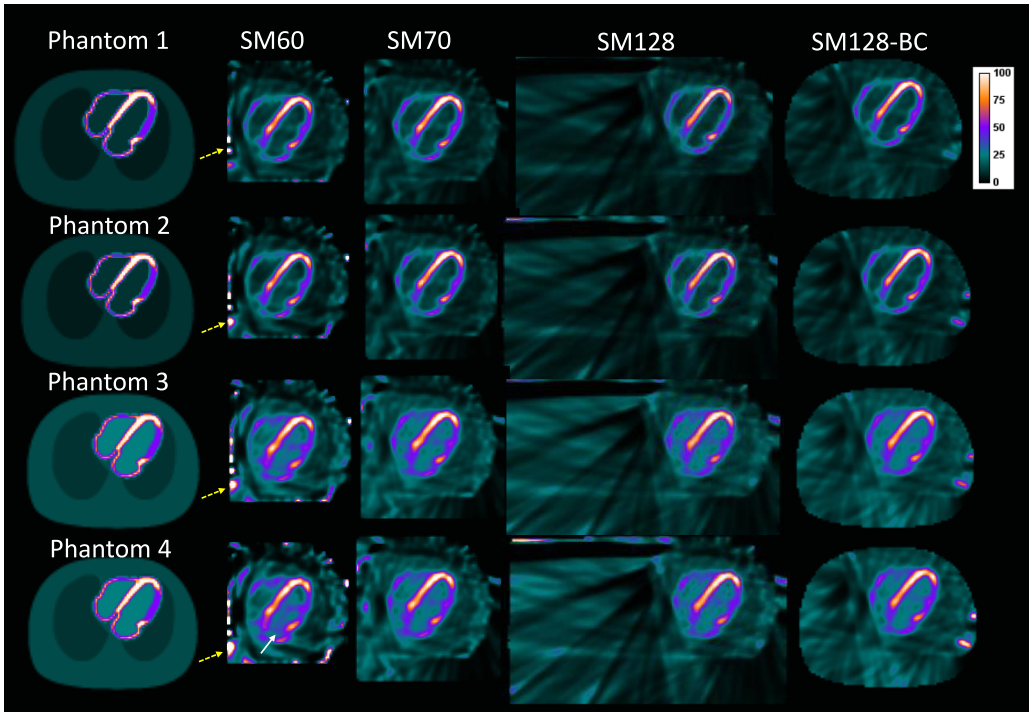

FIG. 4. The central transaxial slices of the reconstructed images using different SM of the noiseless NCAT phantom. All the images were reconstructed with 100 iterations. The yellow dashed arrows denote the artifacts on the edge of the FOV. The white solid arrows denote the artifacts in the blood pool.

the myocardium, all SMs performed similarly for phantom 1. However, SM60 (-Δ-) yielded a gradually increasing CoV with the increased background activity in phantoms 2–4. The bias of the mean activity remains under 5% for the SMs. In the defect ROI, SM60 yielded the highest CoV for a fixed amount of bias among all the SMs, and the differences again increased with the increase of the background activity. SM70 (-◇-) and SM128 (-×-) also yielded higher CoV than SM128-BC (-*-) in phantoms 2–4. In addition, SM128 yielded a slight underestimation compared with the other SMs. In contrast to myocardium and defect regions, SM60 yielded both higher bias and CoV on all the phantoms in the blood pool region, with larger bias on phantoms 1 and 2 than phantoms 3 and 4. This could be because phantoms 1 and 2 had lower activity in the blood pool and thus were more vulnerable to projection truncation. In all the regions, SM128-BC yielded the smallest bias and CoV compared with the other system matrices, and the results were consistent for all of the levels of background activity simulated. The results also suggest that the small SM reconstructions mainly affected quantifications and uniformity of uptake in the relatively low uptake regions in the image.

A summary of the quantification in each ROI for phantoms 2 and 4 reconstructed with 100 iterations is shown in Tables II and III. It can be seen for this number of iterations, SM128-BC reduced the bias by 15% and CoV by 7% in the blood pool compared to SM60 reconstruction for phantom 2 and reduced the bias by 11% and CoV by 7% in the blood pool for phantom 4. SM128-BC yielded the best performance in all regions of each phantom, albeit the improvements over SM70 and SM128 were of a smaller magnitude.

3.B. Patient studies

Figure 6 shows the reconstructed SPECT images in a patient following injection with ^{123}I-mIBG. It can be seen that the SM70 (the default SM) reconstruction produced high activity next to the right ventricular myocardium (denoted by the solid arrow), which was alleviated in the SM150-BC reconstruction. The activity in the blood pool is also lower in the SM150-BC compared with the SM70 reconstruction.

Figure 7 shows a representative stress myocardial SPECT perfusion study in patient injected with ^{99m}Tc-tetrofosmin. This patient was diagnosed with a permanent scar in the inferior wall (as denoted by the solid arrows). With the SM70 reconstruction, the scar appears diminished and connected with background activity on both VLA and SA images, which could be due to the overestimation of the activity in the defect region, as demonstrated in the phantom study. Using the SM150-BC reconstruction, the defect can be more clearly delineated.

Figure 8 shows a representative stress myocardial SPECT scan from a normal patient injected with ^{99m}Tc-tetrofosmin. It can be seen that the SM70 reconstruction yielded images with artifacts near the apex (denoted by the solid arrows), which was alleviated by the SM150-BC reconstruction. Note that high intensity values can be seen on the diagonal boundary in the VLA view in the SM150-BC reconstruction. This is due to the truncation in the axial direction caused by the limited FOV of the attenuation CT.

Figure 9 shows a myocardial SPECT scan of a normal volunteer injected with ^{123}I-mIBG. In this patient, increased uptake can be seen on the edge of the FOV which was

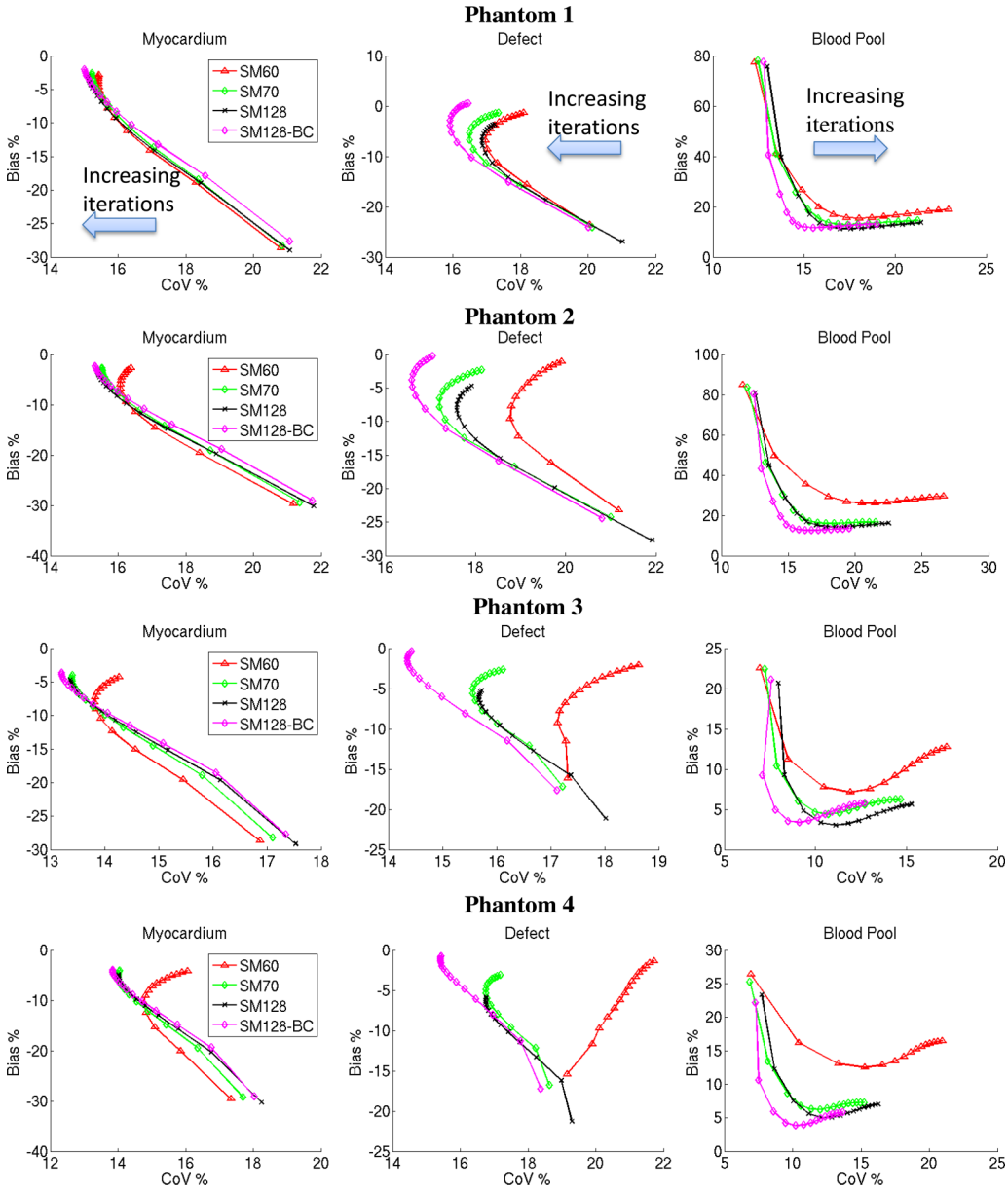

FIG. 5. The bias (%) vs CoV (%) plots from the simulated phantoms. Each data point on the curves represents an increment of 10 iterations.

alleviated in the SM 150-BC reconstruction. Note that the areas of increased activity close to the lateral myocardium in the transaxial and HLA views are reduced in the SM150-BC reconstruction. These differences are probably due to overestimation of the activity in the lung in the SM70 reconstruction.

Figure 10 presents the mean activity measured in the myocardium, blood pool, and the myocardium-to-blood pool contrast averaged across 18 patient studies. It can be seen that SM70 and SM150-BC yielded similar quantitative results in the myocardium. However, the SM70 reconstruction produced significantly higher ($p < 0.0001$) activity in the left blood pool,

TABLE II. Regional bias (%) yielded by different system matrices at the 100th iteration for phantoms 2 and 4. The best performance is highlighted in bold.

	Phantom 2			Phantom 4		
Bias (%) at 100th iteration	Myocardium	Defect	Blood pool	Myocardium	Defect	Blood pool
SM60	−4.6	−3.0	27.5	−6.0	−3.3	15.6
SM70	−4.5	−3.7	16.1	−5.8	−4.1	7.0
SM128	−5.1	−6.3	14.6	−6.7	−7.1	6.3
SM128-BC	**−4.0**	**−1.8**	**12.6**	**−5.7**	**−1.9**	**5.1**

TABLE III. Regional CoV (%) yielded by different system matrices at the 100th iteration for phantoms 2 and 4. The best performance is highlighted in bold.

	Phantom 2			Phantom 4		
CoV (%) at 100th iteration	Myocardium	Defect	Blood pool	Myocardium	Defect	Blood pool
SM60	16.1	19.5	23.8	15.3	21.2	19.4
SM70	15.6	17.6	19.0	14.0	16.8	13.8
SM128	15.5	17.6	19.8	14.1	16.8	14.9
SM128-BC	**15.4**	**16.7**	**17.2**	**13.8**	**15.4**	**12.4**

which led to a lower myocardium-to-blood pool contrast ($p < 0.0001$) by 7% in average (range 0%–18%) across 18 patient studies (rest and stress).

4. DISCUSSIONS

In this study, we have investigated the impact of SM dimension on the reconstructions for a dedicated cardiac SPECT system with multiple CZT detectors and pinhole collimators, and a small focused FOV that can yield truncated projections. We first simulated a generic system that was modeled after a currently available system, imaging phantoms with various levels of extracardiac activity. We then compared the reconstructions achieved using a large SM constrained by CT-derived body contours against the system default SM in 18 patient studies (including images from normal volunteers and patients with and without perfusion defects) acquired on a commercial hybrid SPECT/CT scanner (Discovery NM/CT 570c, GE Healthcare). Our results suggest that using the body contour in the reconstruction could reduce artifacts associated with extracardiac activity, and more importantly, improve image quantification, particularly in low-activity regions.

The results of NCAT simulations showed that projection truncation mainly introduced artifacts on the edge of the FOV, as well as led to overestimation of the activity and nonuniformity in the low activity regions, such as in the region of a perfusion defect and the left ventricular blood pool. The extent of deterioration depends on the combination of the level of extracardiac activity and the relative size of the SM to the body. For example, SM60 yielded up to 27% overestimation in the blood pool for phantom 2. By expanding the SM to SM70, this overestimation was reduced to 16.1%. Although further expanding the SM to SM128 further reduced this overestimation to 14.6%, it also yielded larger underestimation in the myocardium (−5.1%) and defect (−6.3%) than other SMs. This underestimation might be attributed to the fact that the counts were back-projected beyond the body while the total number of counts in the projection was preserved in MLEM intrinsically. Constraining the back-projection with a CT-derived body contour (SM128-BC) yielded the best performance in image quantification and consistently artifact free results inside the FOV on all the phantoms, regardless of the level of extra-cardiac activity. Note although SM60 is not used in clinical systems, this simulation could reflect the results of patients with a large lateral thorax width imaged on this scanner. On the other hand, the results show that the impact on the high activity region inside the FOV (i.e., myocardium) were subtle on all the SM investigated.

Our analyses comparing the different reconstruction approaches in 18 patient studies with and without defects were in line with the findings of the simulation studies. Using a large SM and body contour in reconstruction alleviated extracardiac artifacts and significantly ($p < 0.0001$) improved the average myocardium to blood pool contrast ratio. The contrast improvement was mainly attributed to the reduced activity in the blood pool, whereas the difference in the

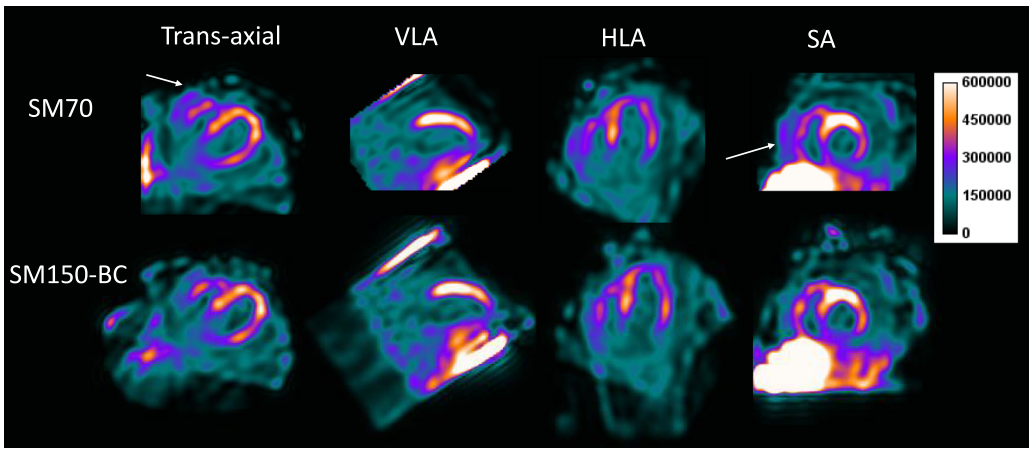

FIG. 6. A sample rest study of a normal patient injected with ^{123}I-mIBG is shown in the standard views. The solid arrows denote the artifact introduced by small SM reconstruction from data with projection truncation.

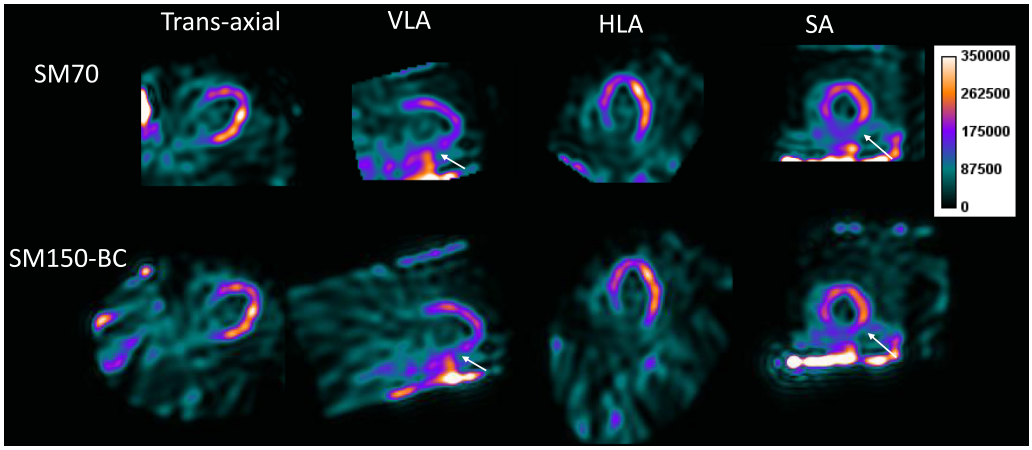

FIG. 7. Representative stress myocarial SPECT perfusion study of a patient with inferior scar (denoted by the arrows) following injection with ^{99m}Tc-tetrofosmin. Images are shown in the standard views.

myocardium was insignificant. The improvements were more prominent in the patients with higher uptake in organs like the liver and gastrointestinal tract located adjacent to the heart. For the scans where extracardiac activity was similar or lower than in the myocardium, the differences between regular SM (SM70) and SM150-BC were subtle. Extracardiac activity could vary vastly across scans even on the same patient due to a combination of factors such as physiological differences at the time of radiotracer injection, as with stress and rest imaging, differences in injected dose (low dose versus high dose), the wait time between injection and scanning, and the positioning of the patient on the scanner. Reliable and consistent reconstruction in the setting of increased extracardiac activity is important for myocardial rest and stress SPECT perfusion studies where these paired studies are used to differentiate between normal perfusion, reversible ischemia, and permanent scar. For the patient studies, although no untruncated data was available as ground truth, the results demonstrate that the image quality from this small FOV CZT SPECT scanner might be improved by using large SM and CT-based body contour in the reconstruction, especially for those patients with high extracardiac activity.

Note that for patient studies reconstructed with SM150-BC, the images were still truncated in the axial direction. This caused high level of counts deposited on the edge of the FOV in the axial direction as can be seen in the VLA and SA views in Figs. 6–9. This is due to the fact that the axial FOV of the reconstruction is limited by the FOV of the attenuation CT. However, it has been shown that the deviations caused by projection truncation in the axial direction were negligible for single isotope acquisition and should not affect clinical diagnosis.[16] To alleviate the artifacts caused by projection truncation in the axial direction, one could expand both the SPECT projections and attenuation map in the axial direction for the patients with extremely high liver uptakes; however, this approach requires further investigation. For SPECT-only systems without CT or other transmission scan capability, a rough measurement of the patient body dimension can be used to determine the optimal reconstruction matrix size as an alternative to the body contour approach, although this approach would require a set of system matrices in different dimensions to be preinstalled in the reconstruction workstation. Alternatively, a rough elliptical support can be generated by matching the major

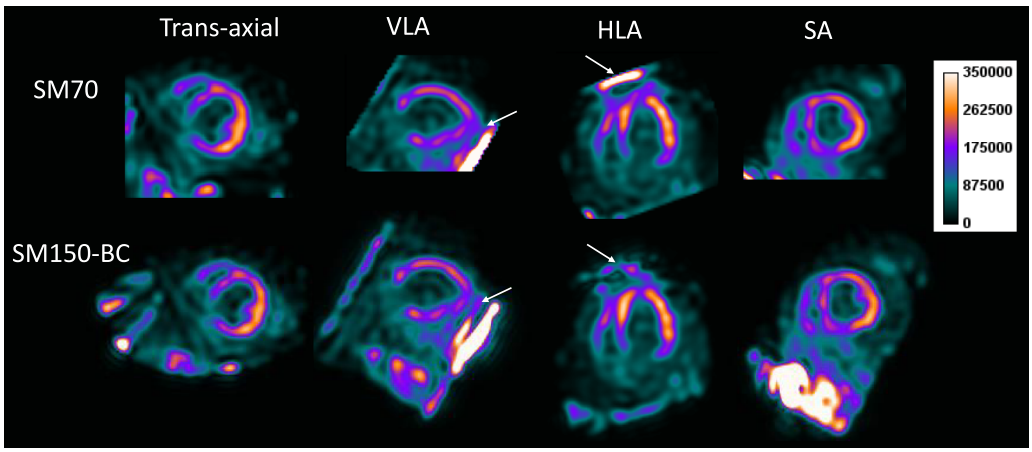

FIG. 8. Representative stress myocardial SPECT perfusion study in a patient injected with ^{99m}Tc-tetrofosmin. Images are shown in the standard views. The arrows denote an artifact near the apex that was alleviated in the SM150-BC reconstruction.

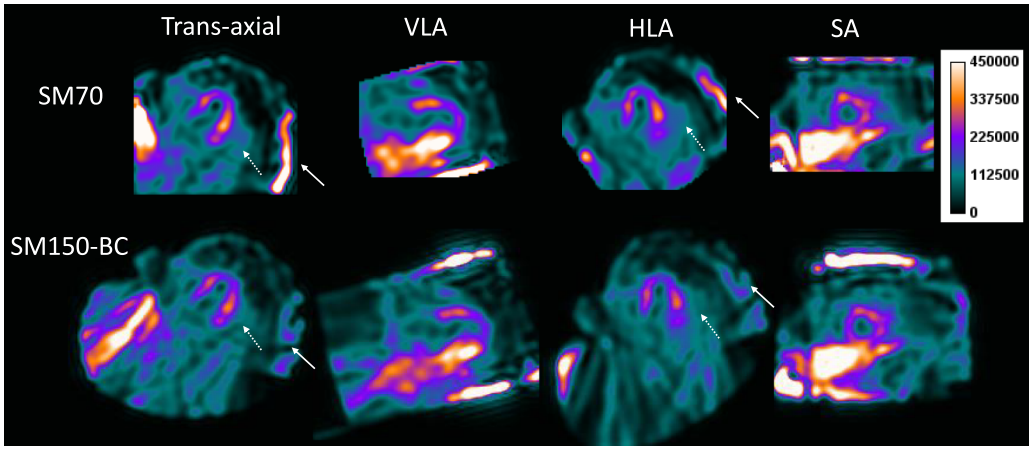

FIG. 9. Representative ^{123}I-mIBG SPECT images from a normal volunteer. Images are shown in the standard views. In this patient, high intensity artifact can be seen on the edge of the FOV (denoted by the solid arrows). The region near the lateral wall (denoted by the dotted arrows) in the transaxial and HLA views also appears to be more blurred in the SM70 reconstruction compared with the SM150-BC reconstruction.

and minor axes with the patient's thorax width and height. The accuracy of body contour would not have a substantial impact on the image quality except when it became 30% larger than the ground truth, as demonstrated in a previous study.[20]

Another potential confounding issue that we did not address in this study was the impact of patient position within the FOV. The positioning of the patient could affect the image quality on this small FOV scanner and could result in different levels of projection truncation based on body habitus. However, as shown in our simulation study, the large SM with body contour yielded consistently superior quantitative results regardless of the level of background activity and was associated with improved image quality among our 18 patient studies with a range of body sizes and patterns of extracardiac activity. Therefore, we expect using large SM with object support could yield more robust and consistent results on patients even with suboptimal patient positioning.

As demonstrated in the simulation studies, reconstruction with body contour substantially reduced bias in the blood pool, which can be a critical factor for achieving absolute quantitative measurement of physiological parameters on this stationary SPECT scanner with dynamic imaging and tracer kinetic modeling.[4,30–32] To illustrate how the method of SPECT image reconstruction might impact on quantitative image analysis, we performed five serial 15-min SPECT scans on one of the human research subjects injected with ^{123}I-mIBG (5.1 mCi). Listmode SPECT imaging (15 min each) was performed at 0, 15, 90, 120, and 180 min after radiotracer injection. Both SM70 and SM150-BC were used in MLEM reconstruction (100 iterations) with attenuation correction for all the 29 dynamic frames rebinned from the five SPECT scans. A two-tissue compartmental model was used for kinetic modeling to obtain the volume of distribution value (V_T) of ^{123}I-mIBG in the myocardium. The details associated with the kinetic modeling for this study can be found in a previous publication.[33] As shown in Fig. 11, the activity in the blood pool was decreased by ~12% in the late phase with our SM150-BC reconstruction compared to the SM70 reconstruction, which was in line with our simulation results. The resulting V_T computed using the SM70 reconstruction was 5.9, while the value using the SM150-BC reconstruction was 7.2, which represents a 22% increase in the V_T. This example study indicated that the SM150-BC reconstruction can generate a more accurate image-derived input function by reducing the background contamination caused by projection truncation and would ultimately result in a more accurate parameter estimation from dynamic SPECT imaging.

The reconstruction employing the body contour also enables partial volume correction (PVC) to be applied on this scanner. As the estimation of background activity is essential in many PVC methods,[34,35] the use of body contour reconstruction could provide a more reliable estimate of

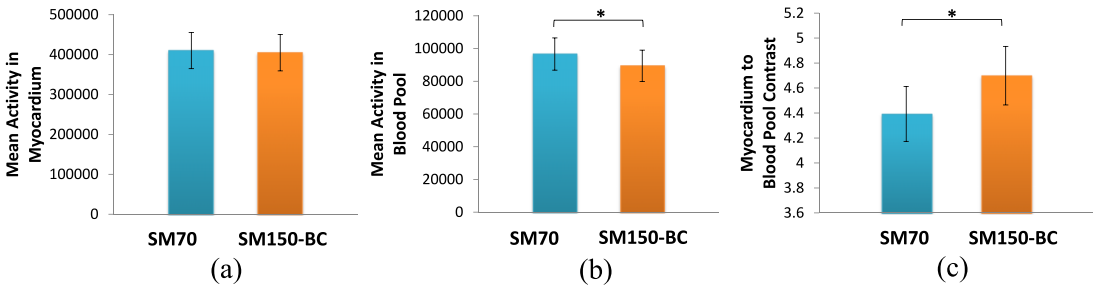

FIG. 10. The mean activity in (a) myocardium and (b) blood pool, averaged across 18 patient studies. (c) The contrast between myocardium and blood pool averaged across 18 patient studies. Error bar: standard error of the mean (SEM). Asterisk (*) denotes $p < 0.0001$.

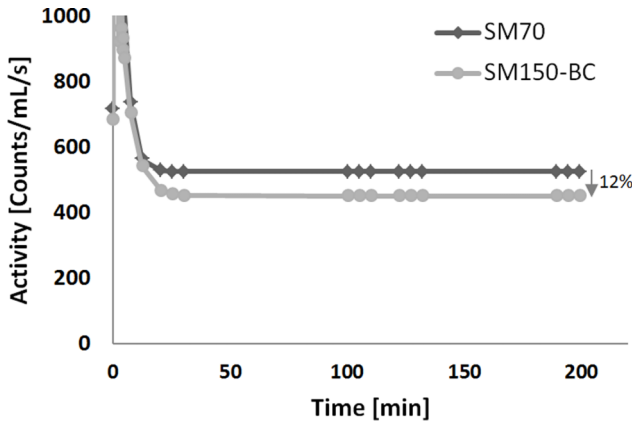

FIG. 11. Image derived arterial input functions (time activity curves from blood pool ROI) derived from blood pool activity on the images reconstructed with SM70 and SM150-BC for a ^{123}I-mIBG dynamic SPECT study.

total counts in the background region, or even the activity in a specific organ outside the FOV. Hence, the use of the proposed large SM and body contour reconstruction might be an essential step to achieve improved quantitative results for these applications.

Finally, in both the simulation and patient studies, we did not observe any adverse effect on the image quality caused by the large SM reconstruction with body contour. However, in addition to the generation of object support or customized system matrix that adapts to patient body size, another potential obstacle for employing this approach in clinical practice might be a higher requirement for the system configuration and reconstruction and result in longer reconstruction times. All the images presented in this work were reconstructed on a workstation equipped with 16 GB of RAM in order to load the large SM, which may not be available in all clinical workstations.

5. CONCLUSIONS

With imaging on a stationary dedicated cardiac small FOV SPECT system with truncated projections, reconstruction with a SM that does not enclose the whole support of the object might lead to artifacts inside the FOV, overestimation in the blood pool activity, and artifactual and nonuniform radiotracer distribution, especially in larger patients with high background activity. Reduced artifacts and the most reliable quantitative results within the FOV might be achieved by using a system matrix that is large enough to contain the entire object and incorporating a CT-derived body contour in support of the reconstruction. Careful selection of SM is particularly important for applications that require quantitative results when acquired on these novel dedicated cardiac CZT SPECT scanners.

ACKNOWLEDGMENTS

This work was funded by a Research Contract from GE Healthcare, American Heart Association Grant-In-Aid Award Nos. 13GRNT17090037, NIH R21HL102574, NIH 1S10RR025555-01, and by CTSA Grant No. UL1 RR024139 from the National Center for Research Resources (NCRR), a component of the National Institutes of Health (NIH), and NIH Roadmap for Medical Research. Its contents are solely the responsibility of the authors and do not necessarily represent the official view of NCRR or NIH. The authors would like to thank Veronica Sandoval and Taraneh Hashemi Zonouz at Yale New Haven Hospital for their assistance in the recruitment of volunteers and data acquisition in the mIBG studies.

[a]Electronic addresses: Chung.Chan@yale.edu and Chi.Liu@yale.edu

[1]E. V. Garcia, T. L. Faber, and F. P. Esteves, "Cardiac dedicated ultrafast SPECT cameras: New designs and clinical implications," J. Nucl. Med. **52**, 210–217 (2011).
[2]P. J. Slomka, J. A. Patton, D. S. Berman, and G. Germano, "Advances in technical aspects of myocardial perfusion SPECT imaging," J. Nucl. Cardiol. **16**, 255–276 (2009).
[3]M. Bocher *et al.*, "A fast cardiac gamma camera with dynamic SPECT capabilities: Design, system validation and future potential," Eur. J. Nucl. Med. Mol. Imaging **37**, 1887–1902 (2010).
[4]R. G. Wells, R. Timmins, R. Klein, J. Lockwood, B. Marvin, R. A. dekemp, L. Wei, and T. D. Ruddy, "Dynamic SPECT measurement of absolute myocardial blood flow in a porcine model," J. Nucl. Med. **55**, 1685–1691 (2014).
[5]C. Chan, M. Harris, M. Le, J. Biondi, Y. Grobshtein, Y.-H. Liu, A. J. Sinusas, and C. Liu, "End-expiration respiratory gating for a high-resolution stationary cardiac SPECT system," Phys. Med. Biol. **59**, 6267–6287 (2014).
[6]S. H. Manglos, G. M. Gagne, and D. A. Bassano, "Quantitative analysis of image truncation in focal-beam CT," Phys. Med. Biol. **38**, 1443–1457 (1993).
[7]D. S. Lalush and B. M. W. Tsui, "Performance of ordered-subset reconstruction algorithms under conditions of extreme attenuation and truncation in myocardial SPECT," J. Nucl. Med. **41**, 737–744 (2000).
[8]R. Clackdoyle, F. Noo, G. Junyu, and J. A. Roberts, "Quantitative reconstruction from truncated projections in classical tomography," IEEE Trans. Nucl. Sci. **51**, 2570–2578 (2004).
[9]S. H. Manglos, "Truncation artifact suppression in cone-beam radionuclide transmission CT using maximum likelihood techniques: Evaluation with human subjects," Phys. Med. Biol. **37**, 549–562 (1992).
[10]G. L. Zeng and G. T. Gullberg, "SPECT region of interest reconstruction with truncated transmission and emission data," Med. Phys. **37**, 4627–4633 (2010).
[11]G. L. Zeng and G. T. Gullberg, "Exact iterative reconstruction for the interior problem," Phys. Med. Biol. **54**, 5805–5814 (2009).
[12]G. K. Gregoriou, B. M. W. Tsui, and G. T. Gullberg, "Effect of truncated projections on defect detection in attenuation-compensated fanbeam cardiac SPECT," J. Nucl. Med. **39**, 166–175 (1998).
[13]T. Zeniya, H. Watabe, T. Inomata, H. Iida, A. Sohlberg, and H. Kudo, "3D-OSEM reconstruction from truncated data in pinhole SPECT," in *IEEE Nuclear Science Symposium and Medical Imaging Conference Record* (IEEE, Honolulu, HI, 2007), Vol. 6, pp. 4205–4207.
[14]T. Zeniya, H. Watabe, A. Sohlberg, T. Inomata, H. Kudo, and H. Iida, "Effect of truncation in quantitative cardiac imaging with small field-of-view pinhole SPECT," in *IEEE Nuclear Science Symposium and Medical Imaging Conference Record* (IEEE, San Diego, CA, 2006), Vol. 6, pp. 3239–3241.
[15]E. Sabondjian, R. Z. Stodilka, T. Belhocine, M. E. King, G. Wisenberg, and F. S. Prato, "Small field-of-view cardiac SPECT can be implemented on hybrid SPECT/CT platforms where data acquisition and reconstruction are guided by CT," Nucl. Med. Commun. **30**, 718–726 (2009).
[16]J. Xiao, F. Verzijlbergen, M. Viergever, and F. Beekman, "Small field-of-view dedicated cardiac SPECT systems: Impact of projection truncation," Eur. J. Nucl. Med. Mol. Imaging **37**, 528–536 (2010).
[17]M. Defrise, F. Noo, R. Clackdoyle, and H. Kudo, "Truncated Hilbert transform and image reconstruction from limited tomographic data," Inverse Probl. **22**, 1037–1053 (2006).
[18]J. E. Bowsher, J. R. Roper, Y. Susu, W. M. Giles, and Y. Fang-Fang, "Regional SPECT imaging using sampling principles and multiple

pinholes," in *IEEE Nuclear Science Symposium and Medical Imaging Conference Record* (IEEE, Knoxville, TN, 2010), pp. 2071–2076.
[19]G. T. Gullberg, G. L. Zeng, F. L. Datz, P. E. Christian, C. H. Tung, and H. T. Morgan, "Review of convergent beam tomography in single photon emission computed tomography," Phys. Med. Biol. **37**, 507–534 (1992).
[20]E. A. Rashed and K. Hiroyuki, "Region-of-Interest reconstruction from truncated projection data under blind object support," in *IEEE Nuclear Science Symposium and Medical Imaging Conference Record* (IEEE, Dresden, Germany, 2008), pp. 3632–3636.
[21]G. L. Zeng and G. T. Gullberg, "Null-space function estimation for the interior problem," Phys. Med. Biol. **57**, 1873–1887 (2012).
[22]Y. Mao and G. L. Zeng, "A tailored ML-EM algorithm for reconstruction of truncated projection data using few view angles," Phys. Med. Biol. **58**, N157–N169 (2013).
[23]J. Dey, "Improvement of performance of cardiac SPECT camera using curved detectors with pinholes," IEEE Trans. Nucl. Sci. **59**, 334–347 (2012).
[24]J. Dey, "Comparing different geometries and reconstruction algorithms for multiple pinhole cardiac SPECT using NCAT," in *IEEE Nuclear Science Symposium and Medical Imaging Conference Record* (IEEE, Valencia, Spain, 2011), pp. 4051–4058.
[25]B. Feng, M. Chen, B. Bai, A. M. Smith, D. W. Austin, R. A. Mintzer, D. Osborne, and J. Gregor, "Modeling of the point spread function by numerical calculations in single-pinhole and multipinhole SPECT reconstruction," IEEE Trans. Nucl. Sci. **57**, 173–180 (2010).
[26]J. A. Kennedy, O. Israel, and A. Frenkel, "3D iteratively reconstructed spatial resolution map and sensitivity characterization of a dedicated cardiac SPECT camera," J. Nucl. Cardiol. **21**, 443–452 (2014).
[27]P. Kailasnath and A. Sinusas, "Comparison of Tl-201 with Tc-99m-labeled myocardial perfusion agents: Technical, physiologic, and clinical issues," J. Nucl. Cardiol. **8**, 482–498 (2001).
[28]B. van der Veen, I. Younis, A. de Roos, and M. M. Stokkel, "Assessment of global cardiac I-123 MIBG uptake and washout using volumetric quantification of SPECT acquisitions," J. Nucl. Cardiol. **19**, 752–762 (2012).
[29]K. Lange and R. Carson, "EM reconstruction algorithms for emission and transmission tomography," J. Comput. Assisted Tomogr. **8**, 306–316 (1984).
[30]C. Liu and A. J. Sinusas, "Is assessment of absolute myocardial perfusion with SPECT ready for prime time?," J. Nucl. Med. **55**, 1573–1575 (2014).
[31]P. Slomka, D. Berman, and G. Germano, "Absolute myocardial blood flow quantification with SPECT/CT: Is it possible?," J. Nucl. Cardiol. **21**, 1092–1095 (2014).
[32]S. Ben-Haim and D. Agostini, "Dynamic SPECT: Evolution of a widely available tool for the assessment of coronary flow reserve," Eur. J. Nucl. Med. Mol. Imaging **42**, 302–304 (2015).
[33]J. Wu, S.-f. Lin, J.-D. Gallezot, Y. Huang, R. Carson, T. Hashemi Zonouz, Y.-H. Liu, R. Lampert, A. Sinusas, and C. Liu, "Quantitative dynamic SPECT imaging of 123I-mIBG in normal human subjects with a population-based plasma metabolite correction," J. Nucl. Med. **56**(Suppl. 3), 1768 (2015).
[34]H. Liu, C. Chan, Y. Grobshtein, T. Ma, Y. Liu, S. Wang, M. Stacy, A. Sinusas, and C. Liu, "Anatomical-based partial volume correction for low-dose dedicated cardiac SPECT/CT," Phy. Med. Bio. **60**, 6751–6773 (2015).
[35]C. Chan, H. Liu, Y. Grobshtein, M. R. Stacy, A. J. Sinusas, and C. Liu, "Simultaneous partial volume correction and noise regularization for cardiac SPECT/CT," in *IEEE Nuclear Science Symposium and Medical Imaging Conference Record* (IEEE, Seoul, Korea, 2013), pp. 1–6.